Linear depth inversion sensitivity to wave viewing angle using synthetic optical video

Linear depth inversion sensitivity to wave viewing angle using synthetic optical video

Eleonora Perugini [a]*, Luciano Soldini [a], Margaret L. Palmsten [b], Joseph Calantoni [b] & Maurizio Brocchini [a]

(a) Dipartimento di Ingegneria Civile, Edile e Architettura, Università Politecnica delle Marche (Ancona, Italia)
e.perugini@pm.univpm.it; l.soldini@univpm.it; m.brocchini@univpm.it;
(b) Marine Geosciences Division, U.S. Naval Research Laboratory (Stennis Space Center, MS USA)
margaret.palmsten@nrlssc.navy.mil; Joe.Calantoni@nrlssc.navy.mil.

Declarations of interest: none.

Abstract

The accuracy of bathymetry estimated by optical implementations of remotely sensed depth inversion algorithms is in part related to the presence of optical wave signal in the images, which depend nonlinearly on the water surface slope. The signal to noise ratio in video images of waves decreases under large azimuthal angles between the camera and wave propagation direction, which can result in poor bathymetry estimation. We quantified errors in depth estimation by analysing the sensitivity of the optical implementation of cBathy v1.1, a widely applied algorithm for depth inversion in coastal regions, to wave viewing angle using synthetic tests. We found relative root mean square errors between 0.02 and 0.08 when the azimuthal angle between the camera look direction and wave approach was less than 75°. However, for higher azimuthal angles, the wave signal was dominated by short wavelengths in the optical images lead in larger depth errors (relative root mean square error = 0.2). We also investigated the sensitivity of the initial guess of the wave direction in the nonlinear solution used by the cBathy v1.1 algorithm to estimate water depth. Observed water depth errors caused by wave viewing angle or initial guess of the wave direction are shown in part to be related to errors in the estimates of frequency and wavenumber. The synthetic methodology and the results of the sensitivity analysis can be generalized to test the accuracy of depth estimation in shore-based video monitoring systems, to design future fixed camera coastal video monitoring stations or to drive the choice of the better viewing angles using small Unmanned Aerial Systems (sUAS) using the Matlab Toolbox we developed.

Keywords

Remote Sensing; Depth-inversion method; Bathymetry estimation; Video imaging.

* Corresponding author.
E-mail address: e.perugini@pm.univpm.it, Tel: +39 071 220 4912, Fax: +39 071 220 4525.

1. Introduction

Optical remote sensing techniques, especially video imagery, are widely employed to monitor the coastal evolution [1, 2]. Optical imagery offers the unique capability to collect high volumes of data at high temporal and spatial resolution with relatively low cost and over long periods. The underlying concept of video imaging in coastal regions is that any visually discernible physical phenomenon can be investigated [1, 2]. Since many nearshore processes have optical signatures, video-monitoring techniques provide useful indirect measurements of the nearshore hydrodynamic and morphological processes.

Waves are imaged as sunlight reflected from the sloped sea surface reaches the camera sensor and is recorded as image intensity. The radiance reaching the camera sensor from a point on the sea surface, I, depends on the sky conditions, the light reflected off the sea surface, as well as the light upwelled from below the sea surface [e.g. 3, 4, 5, 6]. The variation of the wave slope between wave crests and troughs produces the main time-dependent signal in optical imaging of surface gravity waves. I can be expressed as the sky radiance distribution, L, modified by the Fresnel reflection coefficient, R,

$$I = L\,R, \tag{1}$$

where L depends on the brightness of the sky and of the angle of incidence of the light. The sky radiance distribution may be modelled in different ways for different sky conditions [7]. In this manuscript, we consider a uniform sky condition for simplicity, which is equivalent to considering only the Fresnel coefficient, R, [5],

$$I = R = \frac{1}{2}\left[\frac{\sin^2(\omega - \omega')}{\sin^2(\omega + \omega')} + \frac{tan^2(\omega - \omega')}{\tan^2(\omega + \omega')}\right]. \tag{2}$$

The Fresnel reflection coefficient describes the reflectivity of the surface for an unpolarised illumination source where ω is the angle of incidence of the sky radiance with respect to the sea surface normal. Therefore, ω is equal to the angle of the camera viewing direction with respect to the sea surface normal, while ω' is the angle of refraction related to ω by Snell's law, $\sin(\omega) = 1.34 \sin(\omega')$. The sea surface can be defined by the local wave slope, hence it is possible to calculate the vector normal to the wave sea surface,

$$r_n = \frac{r_n'}{\|r_n'\|}, \text{ where } r_n' = \left[\frac{\partial\eta}{\partial x}, \ \frac{\partial\eta}{\partial y}, 1\right]. \tag{3}$$

The camera viewing direction,

$$r_c = [-\cos\tau\cos\alpha_c, \ -\cos\tau\sin\alpha_c, \ \sin\alpha_c], \tag{4}$$

depends on both camera tilt from horizontal, τ, and azimuth, α_c, where the latter is measured from the x-axis in the counter-clockwise direction. Therefore, the incident ray, r_i, can be defined knowing the surface normal and the extrinsic camera parameters as,

$$r_i = 2r_n(r_n \cdot r_c) - r_c. \tag{5}$$

Then, the incidence angle, ω, can be defined as[3],

$$\omega = \cos^{-1}(r_n \cdot r_c). \tag{6}$$

The highest optical contrast occurs when the camera looks in the direction of wave propagation ($\theta - \alpha_c = 0°$, where θ is the incident wave direction), while the waves are less visible when the camera looks along the crest ($\theta - \alpha_c = 90°$), where surface gravity wave slope is less than the direction of propagation. Images looking along the wave crest may be dominated by high frequency waves rather than the dominant component of the wave spectrum [3, 4].

The loss of wave signatures in the images may influence many algorithms that exploit imaging of waves. One of the most important morphological measurements that can be derived from optical determination of wave characteristics is the nearshore bathymetry. The importance of nearshore bathymetry stems from its influence on nearshore physical processes. For example, prediction skill of forecasting models increases with more accurate bathymetric boundary conditions [e.g. 8, 9, 10]. Quantifying bathymetric change is crucial to understand flood risk exposure [11] and erosion and accretion processes of the beach, as well as to support navigation and engineering projects. Monitoring the beach behavior under both seasonal and extreme events is also important to facilitate coastal management decisions [12]. Yet, traditional methods for surveying nearshore bathymetry are expensive and time-consuming, resulting in spatial and temporal resolution lower than necessary for observational and modelling needs. On the contrary, remote sensing techniques can indirectly estimate the water depth and fill spatial and temporal gaps in surveyed bathymetry [13].

Depth-inversion is one of the most frequently used video-based remote sensing methods to estimate nearshore bathymetry in the presence of surface gravity waves. The method is based on the inversion of the dispersion relationship and exploits the wave celerity observed by optical imagery in intermediate or shallow water depths. This approach is based on the linear [e.g. 14], nonlinear [e.g. 15], or extended Boussinesq dispersion equations [e.g. 16]. Wave celerity estimates needed for the inversion can be conducted in the time domain [e.g. 17] or the frequency domain [e.g. 14]. The temporal method computes a time-domain cross-correlation between neighboring positions to estimate the wave celerity [17], while the spectral method uses a cross-spectral correlation to estimate the wave celerity [18]. Both approaches result in depth estimates with similar accuracy using synthetic optical video data [19].

Optical applications of remotely sensed depth inversion methods require video images of waves. Therefore, accuracy of the bathymetric estimation depends partly on the ability to distinguish the wave signal, which is dependent on viewing angle. Typically, shore based video monitoring stations have a fixed azimuthal direction that is nominally in the direction of wave propagation. However, shore based monitoring stations mounted at atypical locations (e.g., cameras mounted on a jetty, headland, or satellite video and unmanned aircraft system (UAS) looking perpendicular to the direction of wave propagation) may result in optical image with a lower signal to noise ratio.

The effects of azimuthal viewing angle on depth inversion algorithms are not documented in literature; therefore, this Short Communication aims to quantify the sensitivity of a widely used depth inversion algorithm, cBathy, to the wave-viewing angle. We chose to conduct the analysis using synthetic data to avoid the complexities of real imagery such as breaking waves, irregular bathymetry, currents, non-uniform lighting conditions and, sometimes, reflection or diffraction of waves and interaction with engineered structures, such as harbors and jetties that violate assumptions of cBathy. Synthetic tests simplify the problem and focus the analysis on the role of light reflection off the water surface and wave viewing angle on error in estimated water depth as well as estimated frequency and wavenumber. The method for creating synthetic imagery is presented in Section 2 along with a review of the cBathy algorithm. In Section 3, we illustrate the application of synthetic tests to study the influence of wave viewing direction on water depth estimation and we discuss the results and the role of errors in frequency and wavenumber. General conclusions are provided in Section 4. In the appendix A we discuss the sensitivity of cBathy v1.1 to the initial guess of the wave direction necessary for the nonlinear solver. Additionally, we provide a freely available toolbox for generating synthetic imagery, so that users can generalize results to their own coastal video monitoring stations.

2. Methods

The procedure used to build synthetic data consists in four main steps. First, frequency-directional spectra are defined. Then, synthetic sea surface elevation time series are generated based on the previously defined input spectra. Afterwards, a time series of synthetic imagery from simulated reflected radiance are built for the simulated sea surface [7, 20]. Finally, the synthetic optical time series are used as input to a widely used depth inversion algorithm to estimate the bathymetry. The Matlab© functions we developed to model the synthetic optical time series, based on the work of Chickadel [21], are available (https://github.com/Coastal-Imaging-Research-Network/station-design-toolbox).

2.1 Synthetic imagery

We considered two types of input spectra to generate the synthetic imagery that included real spectra (Table 1) representative of protected seas (e.g., Adriatic Sea), characterized by bi-modal spectra [22], and analytic frequency-directional spectra (Table 2) to analyze different conditions (different camera height, tilt or spreading parameter). The first type of spectra used to develop synthetic imagery comes from the EsCoSed field experiment, performed at the Adriatic Sea [23], and are representative of the Adriatic winter storm conditions. The observations were collected with a sentinel Acoustic Doppler Current Profile (ADCP) deployed in about 7.3 m water depth and 850 m offshore of the mouth of the Misa River, Senigallia, Italy (43° 43.588' N, 13° 13.941' E). The spectra were statistically estimated from ADCP velocity observations. We focused on a storm that occurred on 25 January 2014, and we selected spectra around the peak of the storm during which the wave height and energy were maximum (E01-E02-E03-E04). Then, we selected one spectrum related to the mean storm energy (E07). We manually modified the peak direction of each selected spectrum, shifting the wave angle but preserving the spectral shape and energy (Figure 1a). In our analyses, the wave propagation direction, θ, is measured from the x-axis (considered the cross-shore direction) in the counter-clockwise direction. The second type of spectra was generated from an analytic frequency-directional spectra, $S(f,\theta)$, which was expressed as

$$S(f,\theta) = E(f)D(f,\theta), \tag{7}$$

where $E(f)$ is the one dimensional, frequency dependent wave spectrum and $D(f,\theta)$ is the directional distribution, which depends on both frequency, f, and direction, θ. The shape of the frequency spectrum ($E(f)$) is defined in terms of the significant wave height, H_s, and the mean zero-upcrossing period, T_z, by fitting the JONSWAP spectrum. For $E(f)$, the formulation of Carter [24] was used, where $T_p = 1.286T_z$ is the spectral peak period,

$$E(f) = G(f)0.0749H_s^2T_z(T_zf)^{-5}\exp\left[-0.4567/(T_zf)^4\right], \tag{8}$$

$$G(f) = 3.3^{\exp\left[-\frac{(1.286T_zf-1)^2}{2\sigma^2}\right]}, \tag{9}$$

$$\sigma = \begin{cases} 0.07 \;\; for \;\; 1.286T_zf < 1 \\ 0.09 \;\; for \;\; 1.286T_zf > 1 \end{cases}. \tag{10}$$

The direction distribution, $D(\theta)$, depends only on the wave direction, θ,

$$\begin{cases} D(\theta) = D_0\cos^{2s}\left[\theta - \theta_P\right] & if \;\; |\theta - \theta_P| < \pi/2 \\ \qquad 0 & otherwise \end{cases}, \tag{11}$$

$$D_0 = \frac{1}{\pi^{0.5}}\frac{\Gamma(s+1)}{\Gamma(s+1/2)}, \tag{12}$$

where θ_P is the spectral peak direction, Γ is the Gamma Function, D_0 is the normalization factor and s is the spreading parameter [25, 26]. The parameters used for the analytical spectra are summarized in Table 2 and an example of the resulting frequency-directional spectra is shown in Figure 1b. We define two general cases, characteristic of the Central Adriatic wave climatology, but the results may be generalized for other sites. The first case used $\mathrm{H_s} = 3.0\ \mathrm{m}$ and $\mathrm{T_p} = 7\ \mathrm{s}$, typical of storm waves in the Adriatic approaching the Italian coast from ESE (A10-A11-A12-A13). The second case used $\mathrm{H_s} = 2.5\ \mathrm{m}$ and $\mathrm{T_p} = 10\ \mathrm{s}$, typical of storm waves approaching from NNE (A20 A21-A22-A23). We generated wave spectra for a range of peak directions.

For each defined spectrum, synthetic sea surface time series have been generated within a simulated camera field-of-view following Percival [27] and Scarsi [26]. The sea surface elevation time series, $\eta(x,y,t)$, can be represented as

$$\eta = i\mathrm{fft}(W), \tag{13}$$

where $i\mathrm{fft}(W)$ is the inverse Fourier transform and the Fourier series, W, is defined as

$$W = A_w(\cos(\varphi) + i\sin(\varphi)) + A_n(\cos(\varphi_n) + i\sin(\varphi_n)), \tag{14}$$

where A_w is the amplitude of the wave signal in the frequency domain and is related to the input spectral characteristics; A_n is the amplitude of the noise signal in the frequency domain and is proportional to the noise to signal ratio, and φ and φ_n are the phase of the harmonic variability of the waves and noise, respectively. Since the spectrum is independent of the phase of the harmonic variability, the phases, φ and φ_n, are arbitrary, hence we computed them with a random function,

$$\varphi = \varphi_r - k\, x\cos\theta - k\, y\sin\theta, \tag{15}$$

$$\varphi_n = \varphi_{r,n}, \tag{16}$$

with random values, $0 \le \varphi_r < 2\pi$, $0 \le \varphi_{r,n} < 2\pi$, and k, the wavenumber. The approach allows for an infinite number of possible time series to be generated with the same input spectrum. We generated a time series for each wave direction, then, we summed for all wave directions. We considered only the real part for the first N_s elements of the transformed series.

Considering the slope of the synthetic sea surface, we generated synthetic optical time series corresponding to the simulated wave time series using the radiance modulation model [7] described in (1) – (6). We simulated optical images of linear, non-breaking waves propagating over a flat bottom in intermediate water depth, where depth inversion algorithms were expected to work well.

2.2 Depth inversion

The optical time series generated in Section 2.1 were used as input to the well-known cBathy v1.1 depth inversion algorithm [28]. We chose this algorithm because itis open source (https://github.com/Coastal-Imaging-Research-Network/cBathy-toolbox) and has become one of the most widely used depth inversion algorithms [e.g. 29, 30, 31, 32, 33, 6, 19, 34, 35, 36].

The cBathy algorithm is based on the inversion of the linear dispersion equation, that relates the water depth to the wave celerity, without a current present,

$$\Omega^2 = gk\,tanh(kh), \tag{17}$$

where Ω is the radian wave frequency, k is the wavenumber, h is the water depth and g is the acceleration due to gravity. The local water depth was estimated from a suite of observed wave frequency and wavenumber pairs. Therefore, accurate bathymetry estimation is dependent upon accurate estimation of both frequency and wavenumber.

Execution of the cBathy v1.1 algorithm consists of three steps. The first step carries out a frequency-dependent analysis and estimates the (usually four) most coherent pairs of wave frequencies and wavenumbers. Following Plant et al. [18], for each analysis point, the algorithm considers a subgrid in which the dominant frequencies are estimated by Fourier transform of the input optical signal and the cross-spectral matrix is computed between all pixel pairs in the subgrid. The cross-spectral matrix is filtered using spatial eigenvector analysis to identify the dominant spatial phase of the waves. The corresponding wavenumbers are derived by fitting the observed spatial phase structure to a forward model. Initial guesses at the value of wavenumber and wave direction (seed angle) are necessary for this nonlinear fit. The second step in the cBathy v1.1 algorithm combines the frequency-wavenumber pairs from Step 1 to give a single depth estimate. At each analysis point, the algorithm chooses the $f - k$ pairs from within the subgrid to use in the depth estimate by weighting by distance from the analysis point and skill of the modelled wave phase. Then, the algorithm calculates the depth as the value that yields the best weighted nonlinear fit between the first step $f - k$ pairs and the dispersion (17). The third step uses a Kalman filter to smooth and average the estimated depth results. The third step is neglected in this analysis.

2.3 Example imagery and depth inversion

An example image and depth inversion is shown for a 1 km by 1 km region with 3 m resolution (Figure 2). The camera height was 25 m and the water depth was constant and equal to 7 m. The camera was located at the origin of coordinate system and looks along the x-direction, but the tilt and azimuth changed over the synthetic image so that the angular difference between the wave and camera view directions varied. In the example imagery, we varied the direction of wave propagation that included, 0° or from the x-direction (Figure 2a and 2d), 90° or from the y-direction (Figure 2c and 2f) and 45° (Figure 2b and 2e).Waves approaching from the x-direction have the convention, $\theta - \alpha_c$ = 0°.

The effects of the variation in camera tilt and camera azimuthal angles on the optical imaging of surface gravity waves were summarized in Section 1. The tilt variation effects manifest as variation of intensity magnitude so that when moving closer to the origin of the camera system, the tilt angle increased and the intensity magnitude decreased (Figure 2a, 2b, 2c). The azimuth variation effects have been observed by changing the wave direction, θ, that is equivalent to changes in azimuth direction, α_c.Qualitatively, synthetic imagery (Figure 2) demonstrates the effect of varying $\theta - \alpha_c$ on both image intensity and bathymetric estimation. By increasing the angular difference, the longer wavelength waves are less visible in the optical image, and wave crests propagating parallel to the viewing direction are dominated by high wavenumbers. Likewise, the estimated water depth is more variable in regions dominated by high wavenumbers which fall closer to the deep water limit. For example, in Figure 2a and 2d, the error was largest close to the y-axis, where the angular difference was maximum (90°), and the error decreases towards the x-axis, where the angular difference was minimum (0°). In Figure 2b and 2e, the bathymetric error was lower because the angular difference did not exceed 45°. In Figure 2c and 2f, the maximum error, corresponding to the maximum angle difference, was close to the x-axis.

3. Results and Discussion

We used the synthetic procedure illustrated in Section 2 to perform a sensitivity analysis of wave viewing direction on water depth estimation. We considered an analysis domain of 200 m by 200 m with 3 m resolution. The camera was located at the origin of coordinate system and looking along the x-direction. Within the domain, we assumed a fixed camera tilt and azimuth angle to focus on the effects of the variation of the azimuthal wave viewing direction. The azimuthal wave viewing angle, $(\theta - \alpha_c)$ was progressively increased from 0° to 90°, by changing the peak wave direction, over the small analysis domain. The camera tilt was set to 14° or 18° and the camera height set to 25 m or 40m, respectively. In one case the tilt was set to 45°. The input bathymetry had a constant depth of 7 m or 10 m. For each combination of input parameters listed in Table 1-2, we computed ten random realizations of the sea surface, optical image, and estimated the water depth, following the methodology outlined in Section 2. Then, for each realization, the relative error in depth estimation was quantified by comparing the estimated bathymetry to the water depth used to create the synthetic sea surface:

$$relative\ error = \sqrt{\frac{\sum_{n=1}^{N} |(h_E - h_T)/h_T|^2}{N}}, \tag{18}$$

where h_E is the estimated water depth and h_T is the true water depth, and N is the number of comparison values (number of grid points). Finally, the mean relative error and the corresponding standard deviation were calculated over the ten realizations to reduce the noise due to the random phases (Figure 3-4). Consistent with our understanding of the effects of azimuthal viewing angle on optical imaging of waves [4, 5], the variation of $(\theta - \alpha_c)$ influenced estimates of water depth.

For analytical spectra, the relative errors for angular differences of less than 75° were almost constant and low (relative error order 0.02 – 0.08) over the horizontal viewing angle variation (Figure 3a, 3b). Within this range of viewing angles, the magnitude of error in bathymetry estimation was consistent with the error reported in observational studies when algorithm assumptions are not violated [14, 6, 34]. For larger angular differences, the waves are looked mainly along the crest and the optical images are dominated by high frequency waves rather than the dominant component of the wave spectrum heading to a noisy signal for the depth inversion algorithm (see Section 1). The presence of short wavelengths in the optical images lead to errors in depth estimation that rapidly increase until a relative error order 0.2 (Figure 3).

Again, using analytical spectra, we considered several other influences on estimated water depth including camera height, camera tilt angle, water depth and directional spreading of the analytical spectra. By considering a specific area of the field of view, changing the camera height is equivalent to changing the tilt angle and vice versa. The camera heights and the relative tilt angles considered here did not affect the general reconstruction of the bathymetry (see differences between case A20 and case A21 in Figure 3a). Considering a fixed camera height and a variable tilt angle is equivalent to modifying the distance from the camera location of the observed area in x direction. We analyzed several values of tilt for a fixed camera height (not shown) but we reported only the case in which the camera looks straight down (A23) because it could be relevant for sUAS. In all cases we did not find any relevant errors on bathymetry estimation in relation to the tilt variation. In fact, in the optical model that we used, the tilt variation affects only the intensity magnitude (Figure 2), which is then normalized by the depth inversion algorithm. The range of waters depths, and normalized water depths (kh) considered here had a minimal effect on the relative depth error, in particular for ($\theta - \alpha_c$) less than 75° (compare cases A20 and case A22 Figure 3a).The water depths were in fact chosen deep enough to avoid breaking and nonlinear effects but not too deep to make the dispersion relationship insensitive to depth. Instead, the directional spreading somewhat affected the depth inversions, particularly as ($\theta - \alpha_c$) increased (Figure 3b). When directional spreading was small, the depth estimate from the inversion was insensitive to ($\theta - \alpha_c$) (see case A13 in Figure 3b).

Error analysis with experimental spectra produced similar results to the analytical spectra (rapidly increasing error for ($\theta - \alpha_c$) greater than 75°), with a few notable differences (Figure 4). Our experimental input spectra were less directionally spread than the analytical spectra. In most cases the error magnitude of the experimental cases was similar to the error magnitude of the analytical cases with low directional spreading (A12-A13). The cases E01, E02, E03, E04 error increases as a function of ($\theta - \alpha_c$) in a way similar to the analytical cases while a different behavior has been observed for case E07 (Figure 4, green line). This last case is characterized by shorter peak wave period, and in turn by larger value of kh, than the other cases (see Table 1). We found that the anomalous shape is related to sampling problems inside the cBathy v1.1 due to the shorter waves of case E07. To avoid this problem, we used the cBathy v1.2 that improves the nonlinear fit for short waves (see Figure 4).

Since the depth inversion estimation depends upon accurate estimates of frequency and wave number pairs, we compared the $f - k$ pairs, estimated from cBathy v1.1, with the linear dispersion relationship relative to the spectrum at the specific depth (Figure 5). The cBathy v1.1 derived frequencies and wavenumbers come from the four most coherent frequency-wavenumber pairs obtained in Step 1 of the algorithm that exceded a minimum skill threshold. Errors in frequency and wavenumber pair estimations increase with increasing the wave viewing angle ($\theta - \alpha_c$) and erroneous frequency and wavenumber pairs begin to dominate for angles exceeding 75°.

4. Conclusions

We utilized synthetic tests to analyze the effects of wave direction on water depth estimation using the optical implementation of the linear depth inversion algorithm, cBathy v1.1. We found that the error in the water depth estimates where wave viewing angle is less than 75° were consistent with previous field observations (relative root mean square error = 0.02 – 0.08). Given that the synthetic tests were designed to adhere to algorithm assumptions, the result suggests the limit of accuracy that can be expected from the algorithm. When the wave viewing angle exceeded 75°, the wave slope associated with the dominant frequencies became obscured, leading to errors in both frequency and wavenumber estimation which in turn result to errors in depth. Errors were larger for directionally spread waves. Our results and the proposed procedure to build synthetic optical images can be applied to develop sampling schemes for fixed camera coastal video monitoring stations or for small Unmanned Aerial Systems (sUAS) with viewing waves different from the typically offshore-pointing azimuth direction.

Acknowledgements

The authors thank Alex Sheremet for shearing measured spectra, Chris Chickadel for sharing Matlab© codes, Carlo Lorenzoni for helping with the wave spectra analyses and Kate Brodie for useful discussions. Financial support from the ONR Global (UK), through the NICOP EsCoSed Research Grant (N62909-13-1-N020) is gratefully acknowledged. M.L. Palmsten and J. Calantoni were supported under base funding to the U.S. Naval Research Laboratory from the Office of Naval Research.

Appendix A

cBathy v1.1 requires an initial guess at the direction of wave propagation to seed the nonlinear fit used to obtain directions and wavenumbers in Step 2 of the algorithm. Therefore, the choice of the seed angle also impacts the final estimate of water depth. Usually, the cBathy v1.1 seed angle is set assuming that the waves come from the cross-shore direction (0°). However, in operational application the incoming wave may not be shore-normal directed and the direction of wave propagation may vary with space and time. As a result, the seed angle is a potential source of error in the estimated water depth using cBathy v1.1. Note that the new version of cBathy algorithm (cBathy v1.2) removes the need to specify the incoming wave angle by estimating the seed angle from the spatial phase structure and an initial guess at water depth. However, the cBathy v1.1 is still widely used and the seed angle problem is not yet addressed in the literature.

To quantify the sensitivity of the cBathy v1.1 to the seed angle, we present results with different initial guesses of the wave direction. This analysis has been performed using the 1 km by 1 km grid (Figure 2) and considering three directions of wave propagation (0°, 45°, 90°). cBathy was initialized using a range of seed angles (from 0° to 90°) and the parameters listed in Table 3. The relative error was computed with (18) (Figure A.1). Differences between seed angle and wave direction greater than 45° resulted in undulatory features in the estimated water depth (not shown) and relative errors order 0.1-0.4 (Figure A.1). Relative error was minimized when the seed angle was closest to the wave direction. In the analyses performed in Section 2-3, we cared to set the initial guess at the direction equal to the wave propagation direction to avoid that the error due to a mistake of the setting seed angle can be added to the error due to a large wave viewing angle.

Finally, we investigated the role of the seed angle in $f - k$ estimated from Step 1 of the cBathy v1.1 algorithm. For this analysis, we compered the linear dispersion relationship with the estimated frequency-wavenumber pairs that exceded a minimum skill threshold in a way similar to the analysis performed in Section 3. Figure A.2 shows an example of this comparison for case E01 and wave direction equal to 0°. For cases with no error in seed angle (Figure A.2a), errors in frequency and wavenumber pair estimations were minimal while the errors increased when the seed angle was not correctly setting (Figure A.2b-c). In the last cases the underestimation of the depth was related to an overestimation of the wavenumber.

References

[1] R. A. Holman, A. H. Sallenger, T. C.Lippmann, J. W.Haines, The application of video image processing to study of nearshore processes, Oceanography, 6 (3) (1993) 78–85. https://doi.org/10.5670/oceanog.1993.02.

[2] K. T. Holland, R. A. Holman, Video Estimation of Foreshore Topography Using Trinocular Stereo. Journal of Coastal Research, 13 (1) (1997) 81–87. http://journals.fcla.edu/jcr/article/view/80106.

[3] D. Stilwell, Directional energy spectra of the sea from photographs, J. Geophys. Res. 74 (8) (1969) 1974–1986. https://doi.org/10.1029/JB074i008p01974.
[4] B. Jähne, J. Klinke, S. Waas, Imaging of short ocean wind waves: a critical theoretical review. J. Opt. Soc. Am. A, 11 (8) (1994) 2197–2209. https://www.osapublishing.org/abstract.cfm?URI=josaa-11-8-2197.
[5] R. E. Walker, Marine light field statistics, Wiley, New York, 1994.
[6] R. A. Holman, K. L. Brodie, N. J. Spore, Surf Zone Characterization Using a Small Quadcopter: Technical Issues and Procedures, IEEE Trans. Geosci. Remote Sens. 55 (4) (2017) 2017–2027. https://doi.org/10.1109/TGRS.2016.2635120.
[7] R. D. Chapman, Visibility of rms slope variations on the sea surface., Appl. Opt. 20 (11) (1981) 1959–1966. https://doi.org/10.1364/AO.20.001959.
[8] L. C. van Rijn, D. J. R. Wasltra, B. Grasmeijer, J. Sutherland, S. Pan, J. P. Sierra, The predictability of cross-shore bed evolution of sandy beaches at the time scale of storms and seasons using process-based profile models, Coast. Eng. 47 (3) (2003) 295-327. https://doi.org/10.1016/S0378-3839(02)00120-5.
[9] R. A. Holman, D. M. Lalejini, K. Edwards, J. Veeramony, A parametric model for barred equilibrium beach profiles, Coast. Eng. 90 (2014) 85-94. https://doi.org/10.1016/j.coastaleng.2014.03.005.
[10] R. A. Holman, D. M. Lalejini, T. Holland, A parametric model for barred equilibrium beach profiles: Two-dimensional implementation, Coast. Eng. 117 (2016) 166–175. https://doi.org/10.1016/j.coastaleng.2016.07.010.
[11] M. W. Beck, I. J. Losada, P. Menéndez, B. G. Reguero, P. Díaz-Simal, F. Fernández, The global flood protection savings provided by coral reefs. Nature Communications, 9 (1) (2018) 1–9. https://doi.org/10.1038/s41467-018-04568-z.
[12] M. Davidson, M. Van Koningsveld, A. de Kruif, J. Rawson, R. Holman, A. Lamberti, R. Medina, A. Kroon, S. Aarninkhof., The CoastView project: Developing video-derived Coastal State Indicators in support of coastal zone management, Coast. Eng. 54 (6–7), (2007) 463–475. https://doi.org/10.1016/j.coastaleng.2007.01.007.
[13] K. T. Holland, M. L. Palmsten, M, Remote Sensing Applications and Bathymetric Mapping in Coastal Environments, Advances In Coastal Hydraulics, 2018, pp. 375-411. https://doi.org/10.1142/9789813231283_0010
[14] H. F. Stockdon, R. A. Holman, Estimation of wave phase speed and nearshore bathymetry from video imagery, J. Geophys. Res. Ocean. 105 (C9) (2000) 22015–22033. https://doi.org/10.1029/1999JC000124.
[15] P. A. Catálan, M. C. Haller, Remote sensing of breaking wave phase speeds with application to non-linear depth inversions, Coast. Eng. 55 (1) (2008) 93–111. https://doi.org/10.1016/j.coastaleng.2007.09.010.
[16] S. K. Misra, A. B. Kennedy, J. T. Kirby, An approach to determining nearshore bathymetry using remotely sensed ocean surface dynamics, Coast. Eng. 47 (3) (2003) 265–293. https://doi.org/10.1016/S0378-3839(02)00118-7.
[17] R. Almar, P. Bonneton, N. Senechal, D. Roelvink, Wave celerity from video imaging: a new method, in Proc. Coastal Engineering 2008, Hamburg, Germany (2009) 661–673. https://doi.org/10.1142/9789814277426_0056.
[18] N. G. Plant, K. T. Holland, M. C. Haller, Ocean Wavenumber Estimation From Wave-Resolving Time Series Imagery, IEEE Trans. Geosci. Remote Sens. 46 (9) (2008) 2644–2658. https://doi.org/10.1109/TGRS.2008.919821.
[19] E. W. J. Bergsma, R. Almar, Video-based depth inversion techniques, a method comparison with synthetic cases, Coast. Eng. 138 (2018) 199–209. https://doi.org/10.1016/j.coastaleng.2018.04.025.
[20] R. D. Chapman, G. B. Irani, Errors in estimating slope spectra from wave images, Appl. Opt. 20 (20) (1981) 3645-3652. https://doi.org/10.1364/AO.20.003645.
[21] C. C. Chickadel, Remote Measurements of Waves and Currents over Complex Bathymetry, PhD Thesis, Oregon State University, 2007. http://ir.library.oregonstate.edu/concern/graduate_thesis_or_dissertations/5h73pz25f.
[22] M. Brocchini, J. Calantoni, A. H. Reed, M. Postacchini, C. Lorenzoni, A. Russo, A. Mancinelli, S. Corvaro, G. Moriconi, L. Soldini, Summertime conditions of a muddy estuarine environment: The EsCoSed project contribution, Water Sci. Technol. 71 (10) (2015) 1451–1457. https://doi.org/10.2166/wst.2015.116.
[23] M. Brocchini, J. Calantoni, M. Postacchini, A. Sheremet, T. Staples, J. Smith, A. H. Reed, E. F. Braithwaite, C. Lorenzoni, A. Russo, S. Corvaro, A. Mancinelli, L. Soldini, Comparison between the wintertime and summertime dynamics of the Misa River estuary, Mar. Geol. 385 (2017) 27–40. https://doi.org/10.1016/j.margeo.2016.12.005.
[24] D. J. T. Carter, Prediction of wave height and period for a constant wind velocity using the JONSWAP results, Ocean Eng. . 9 (1) (1982) 17–33. https://doi.org/10.1016/0029-8018(82)90042-7.
[25] M. Nwogu, O., Mansard, E.P.D., Miles, M., Isaacson, Estimation of directional wave spectra by the Maximum Entropy Method., in Proc. IAHR Seminar on Wave Analysis and Generation in Laboratory Basins, XXII IAHR Congress, Lausanne, Switzerland, (1987) 363–376.
[26] G. Scarsi, Elementi di idraulica marittima e costiera (In italian), ARACNE, Roma, 2009.
[27] D. B. Percival, Simulating Gaussian random processes with specified spectra, Computing Science and Statistics, 534-534, 1993.
[28] R. Holman, N. Plant, T. Holland, CBathy: A robust algorithm for estimating nearshore bathymetry, J. Geophys. Res. Ocean. 118 (5) (2013) 2595–2609. https://doi.org/10.1002/jgrc.20199.
[29] R. Holman, J. Stanley, cBathy Bathymetry Estimation in the Mixed Wave-Current Domain of a Tidal Estuary., J. Coast. Res. 165 (65) (2013) 1391–1396. https://doi.org/10.2112/SI65-235.1.
[30] M. Radermacher, M. Wengrove, J. van Thiel de Vries, R. Holman, Applicability of video-derived bathymetry estimates to nearshore current model predictions, J. Coast. Res. 70 (2014) 290–295. https://doi.org/10.2112/SI70-049.1.
[31] L. Sembiring, A. van Dongeren, G. Winter, M. van Ormondt, C. Briere, D. Roelvink, Nearshore bathymetry from video and the application to rip current predictions for the Dutch Coast, J. Coast. Res. 70 (2014) 354–359. https://doi.org/10.2112/SI70-060.1.
[32] G. M. D. Méndez, M. C. Haller, B. Raubenheimer, S. Elgar, D. A. Honegger, Radar remote sensing estimates of waves and wave forcing at a Tidal inlet, J. Atmos. Ocean. Technol. 32 (4) (2015) 842–854. https://doi.org/10.1175/JTECH-D-14-

00215.1.
[33] E. W. J. Bergsma, D. C. Conley, M. A. Davidson, T. J. O'hare, Video-based nearshore bathymetry estimation in macro-tidal environments, Mar. Geol. 374 (2016) 31-41. https://doi.org/10.1016/j.margeo.2016.02.001.
[34] K. L. Brodie, M. L. Palmsten, T. J. Hesser, P. J. Dickhudt, B. Raubenheimer, H. Ladner, S. Elgar., Evaluation of video-based linear depth inversion performance and applications using altimeters and hydrographic surveys in a wide range of environmental conditions, Coast. Eng. 136 (2018) 147-160. https://doi.org/10.1016/j.coastaleng.2018.01.003.
[35] J. Rutten, S. M. de Jong, G. Ruessink, Accuracy of Nearshore Bathymetry Inverted From *X* -Band Radar and Optical Video Data, IEEE Trans. Geosci. Remote Sens. 55 (2) (2017) 1106–1116. https://doi.org/10.1109/TGRS.2016.2619481.
[36] S. Zuckerman, S. Anderson, Bathymetry and Water-Level Estimation Using X-Band Radar at a Tidal Inlet, J. Coast. Res. 34 (5) (2018) 1227-1235. https://doi.org/10.2112/JCOASTRES-D-17-00182.1.

Table 1 *- Summary of analysed sea states and parameters, from EsCoSed experiment source. For each case the table displays the index, the peak period, the significant wave height, the wave energy, the camera height, the camera tilt angle (fixed in the wave viewing analysis), the water depth and the kh computation.*

case	**Tp** (s)	**Hs** (m)	**Smax** (m^2s)	**hc** (m)	**tilt** (°)	**h** (m)	**kh**
E01	8.79	2.95	10.85	25	14	7	0.6427
E02	8.79	3.09	8.74	25	14	7	0.6427
E03	9.44	2.99	5.31	25	14	7	0.5933
E04	9.44	2.92	14.21	25	14	7	0.5933
E07	5.94	1.54	1.51	25	14	7	1.0304

Table 2 *- Summary of analysed sea states and parameters, from analytical source. For each case the table displays the index, the peak period, the significant wave height, the spreading parameter, the camera height, the camera tilt angle (fixed in the wave viewing analysis), the water depth and the kh computation.*

case	**Tp** (s)	**Hs** (m)	**s**	**hc** (m)	**tilt** (°)	**h** (m)	**kh**
A10	7.00	3.00	5	25	14	7	0.8384
A11	7.00	3.00	2	25	14	7	0.8384
A12	7.00	3.00	10	25	14	7	0.8384
A13	7.00	3.00	20	25	14	7	0.8384
A20	10.00	2.50	5	25	14	7	0.5567
A21	10.00	2.50	5	40	18	7	0.5567
A22	10.00	2.50	5	25	14	10	0.6798
A23	10.00	2.50	5	25	45	7	0.5567

Table 3 *- Summary of cBathy parameters. The x-axis is the cross-shore direction, and the y-axis is the alongshore direction.*

cBathy parameter name	**value**	**desription**
params.dxm	9 m	Analysis domain spacing in x
params.dym	13 m	Analysis domain spacing in y
params.xyMinMax	[0 1000 0 1000] for Grids [50 250 50 250] for Patches	Spatial extent of the analysis grid
params.MINDEPTH	0.25 m	Min limit set for the nonlinear depth search in phase 2.
params.QTOL	0.5	Min skill
params.minLam	10	Min normalized eigenvalue to proceed
params.Lx	2*params.dxm	Smoothing length scales in x
params.Ly	2*params.dym	Smoothing length scales in y
params.kappa0	3	Multiplier that increase Lx seaward
params.maxNPix	80	Max number of pixels per subgrid
params.fB	[1/15 : 1/100 : 1/4]	List of frequencies for analysis
params.nKeep	4	Number of frequencies to keep
params.offshoreRadCCWFromx	Variable	Seed angle

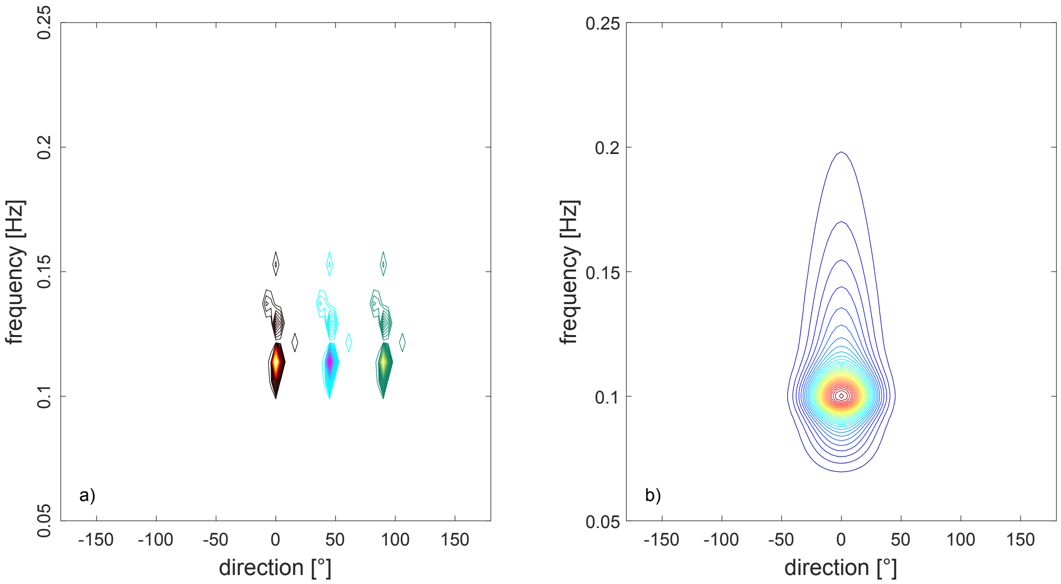

***Figure 1** – a) Example of peak shifting for case E01 with peak directions of 0° (red), 45° (blue), and 90° (green). b) Example of frequency directional spectrum (A20) designed using equations (7) to (12). (For interpretation of the references to color in this figure, the reader is referred to the Web version of this article.)*

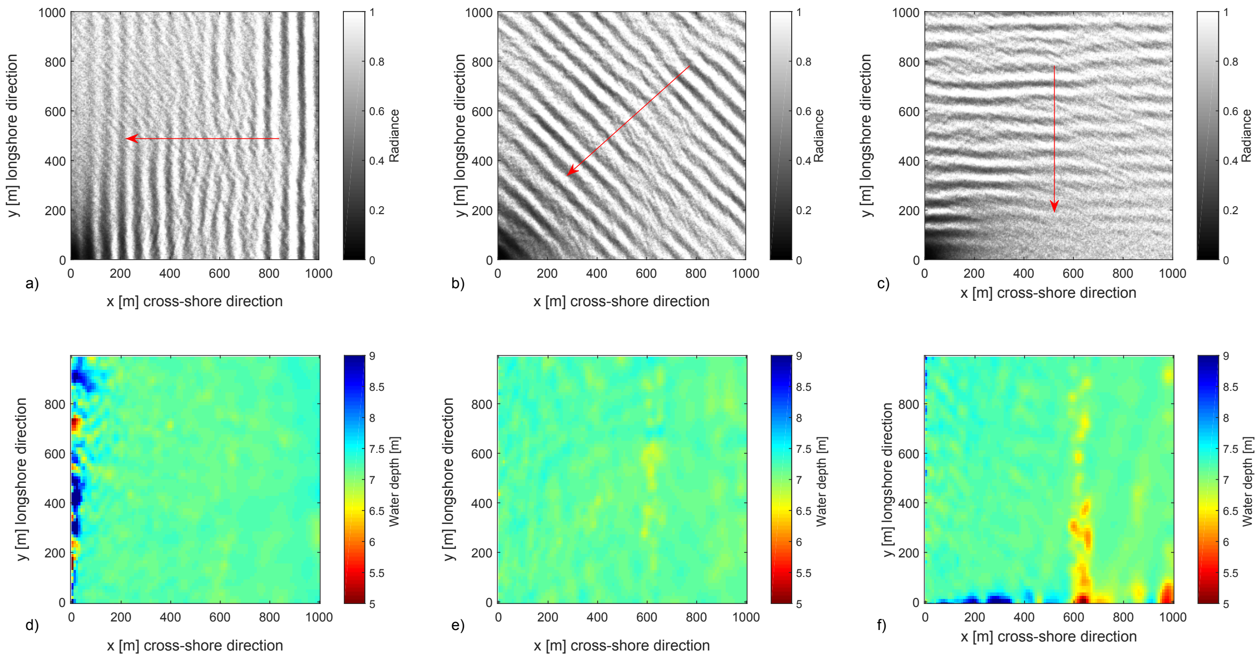

***Figure 2** –Synthetic optical images (upper panels) and estimated bathymetry (lower panels), for case E01, for wave angles equal to 0° (a,d), 45° (b,e), and 90° (c,f). The angles are positive in the counter-clockwise direction from the x-axis. The red arrows indicate the wave direction. The seed angle was set coherent to wave propagation. (For interpretation of the references to color in this figure, the reader is referred to the Web version of this article.)*

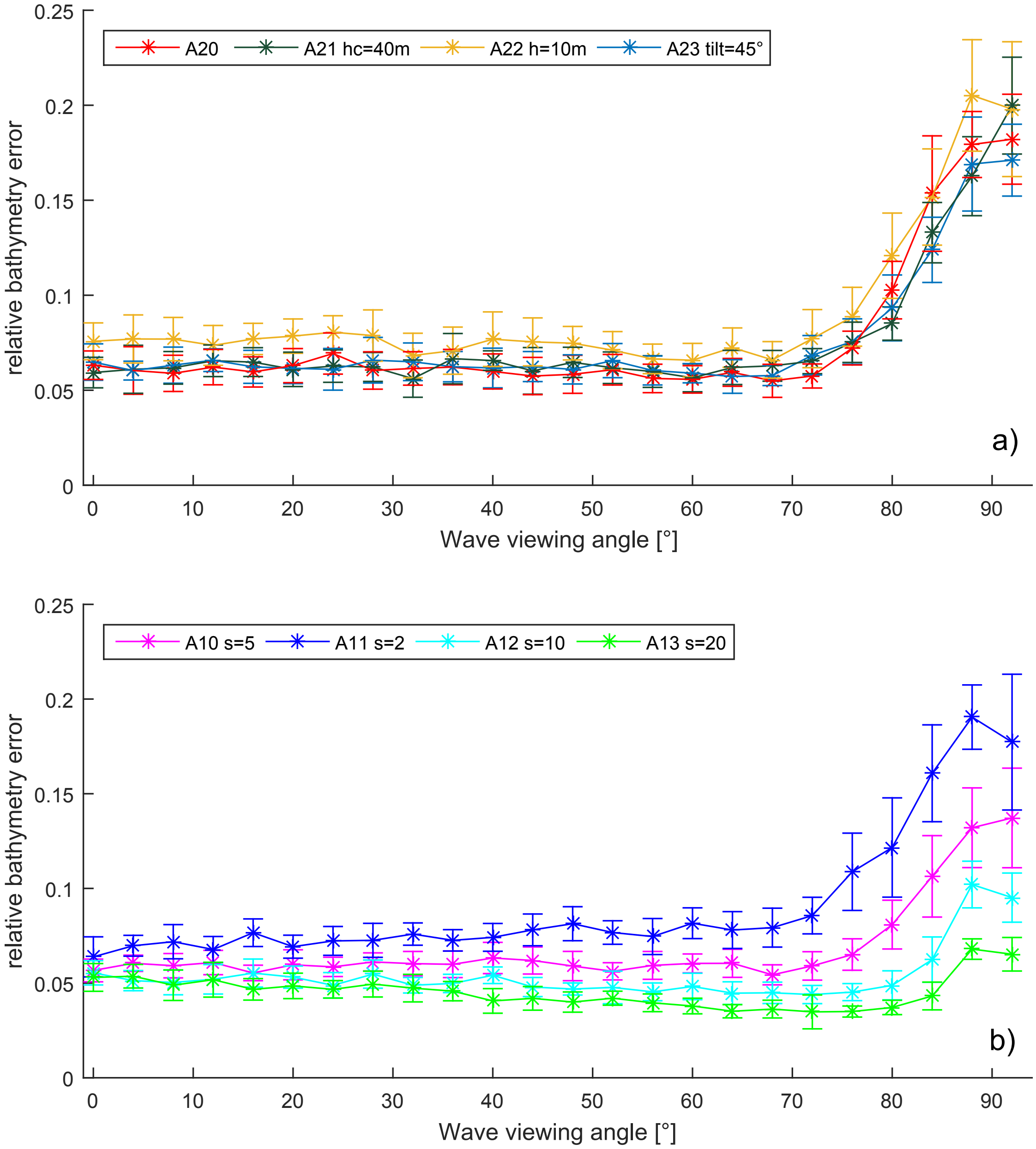

Figure 3 *- Mean (*) and standard deviation (bars) of bathymetric error as function of difference between wave angle and camera viewing direction. a) analytical spectra A20, A21, A22 and A23; b) analytical spectra A10, A11, A12 and A13 with different directional spreading. (For interpretation of the references to color in this figure legend, the reader is referred to the Web version of this article.)*

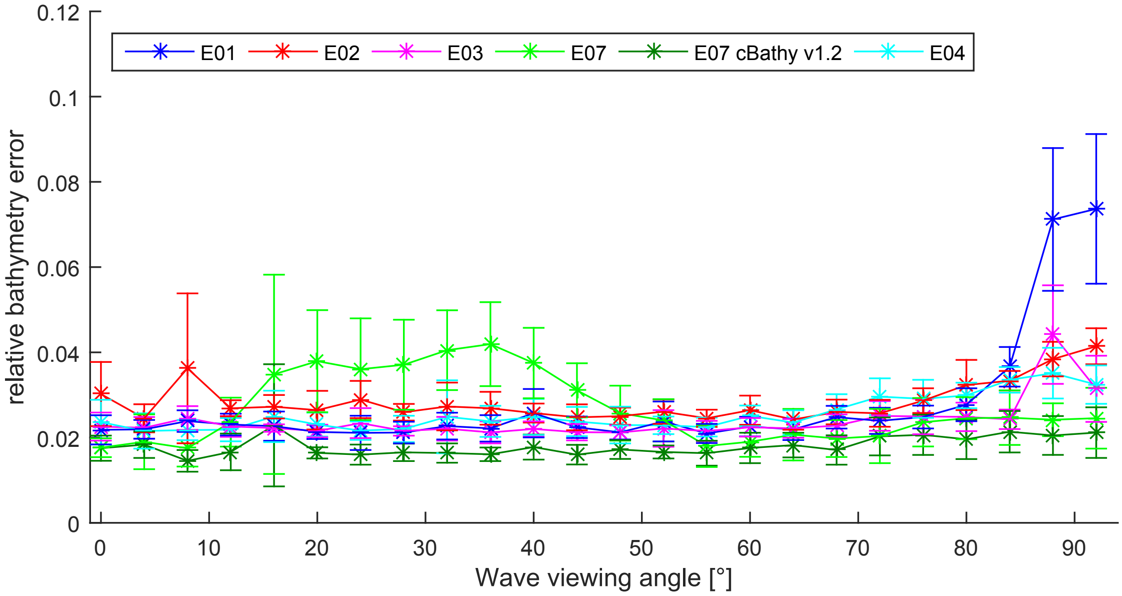

Figure 4 *- Mean (*) and standard deviation (bars) of bathymetric error as function of difference between wave angle and camera viewing direction for observed spectra E01, E02, E03, E04 and E07. (For interpretation of the references to color in this figure legend, the reader is referred to the Web version of this article.)*

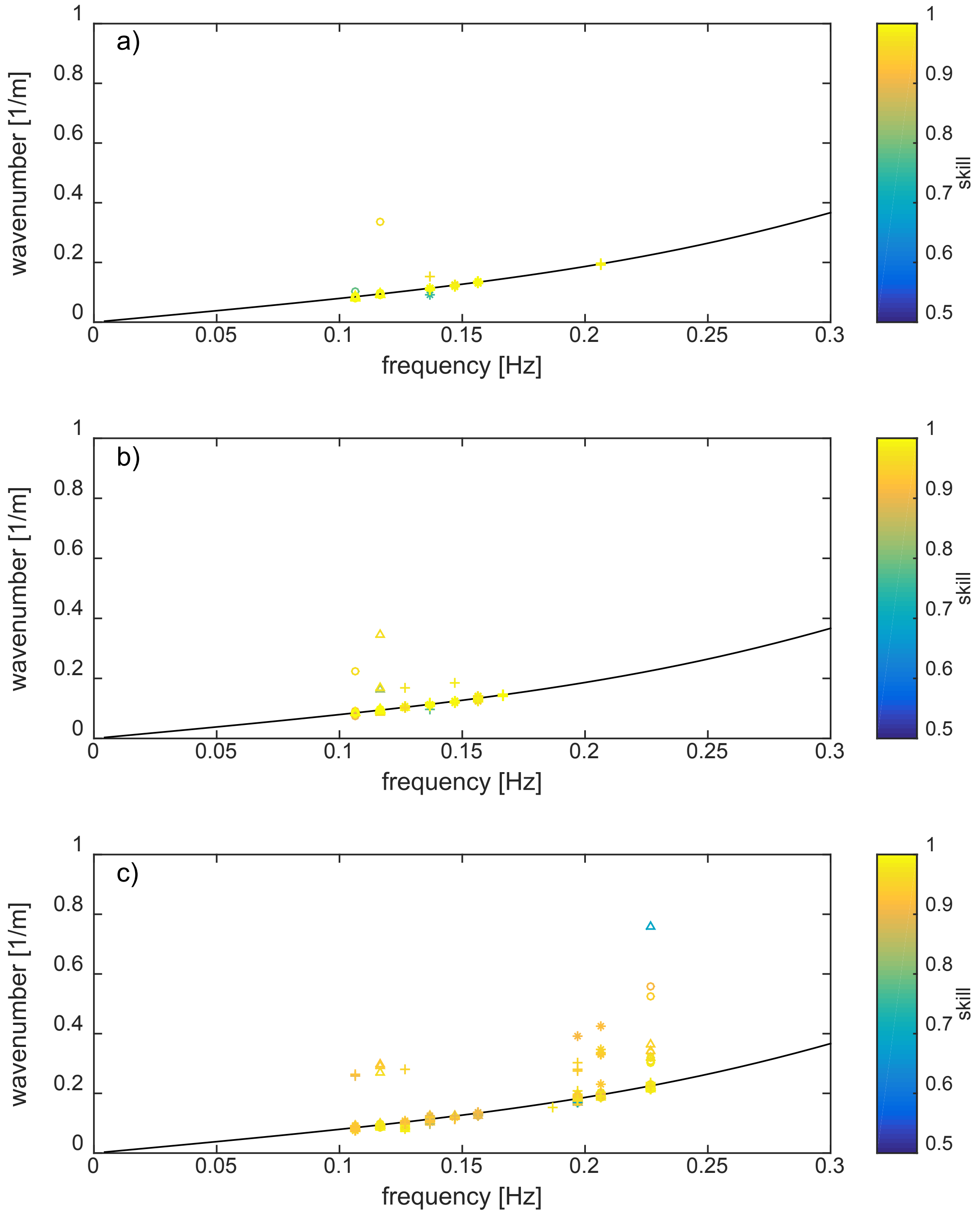

Figure 5 *–Frequency and wavenumber pairs estimated from cBathy for case E01 and relative to waves coming from 0° (a), 44° (b) and 92° (c). The curve shows the linear dispersion relationship for the specified water depth (7m). The markers indicate the f-k pairs estimated from cBathy in each point of the analysis grid and relative to the first (•), the second (△), the third (*) and the fourth (+) coherent frequency. The color gradient of the markers is proportional to the skill but only points that exceed the threshold are plotted. Only one of the ten realizations is plotted for illustration. (For interpretation of the references to color in this figure legend, the reader is referred to the Web version of this article.)*

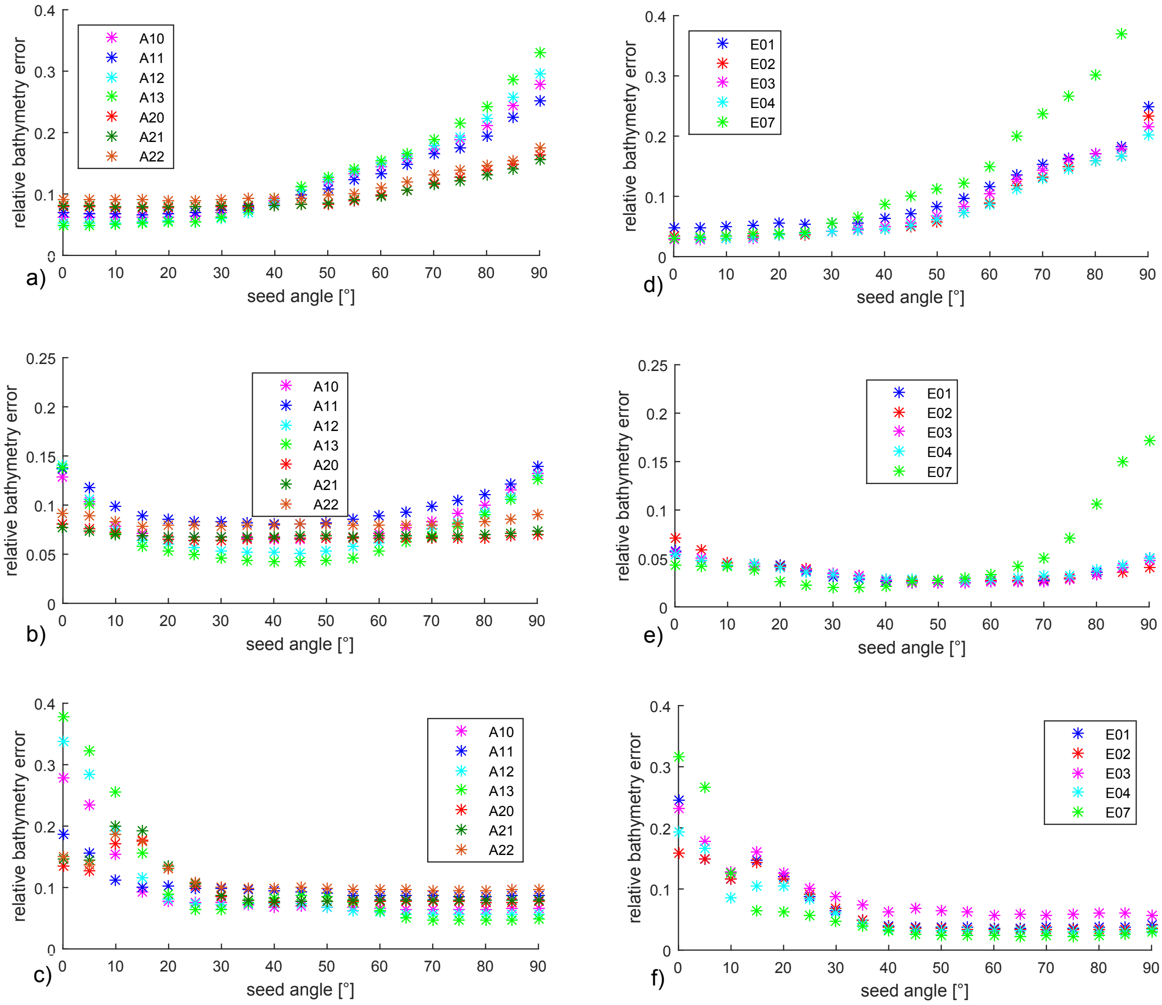

Figure A.1– *Seed angle sensitivity for analytical (a-b-c) and experimental (d-e-f) cases with wave angles of 0° (a,d), 45° (b,e), and 90° (c,f). (For interpretation of the references to color in this figure legend, the reader is referred to the Web version of this article.)*

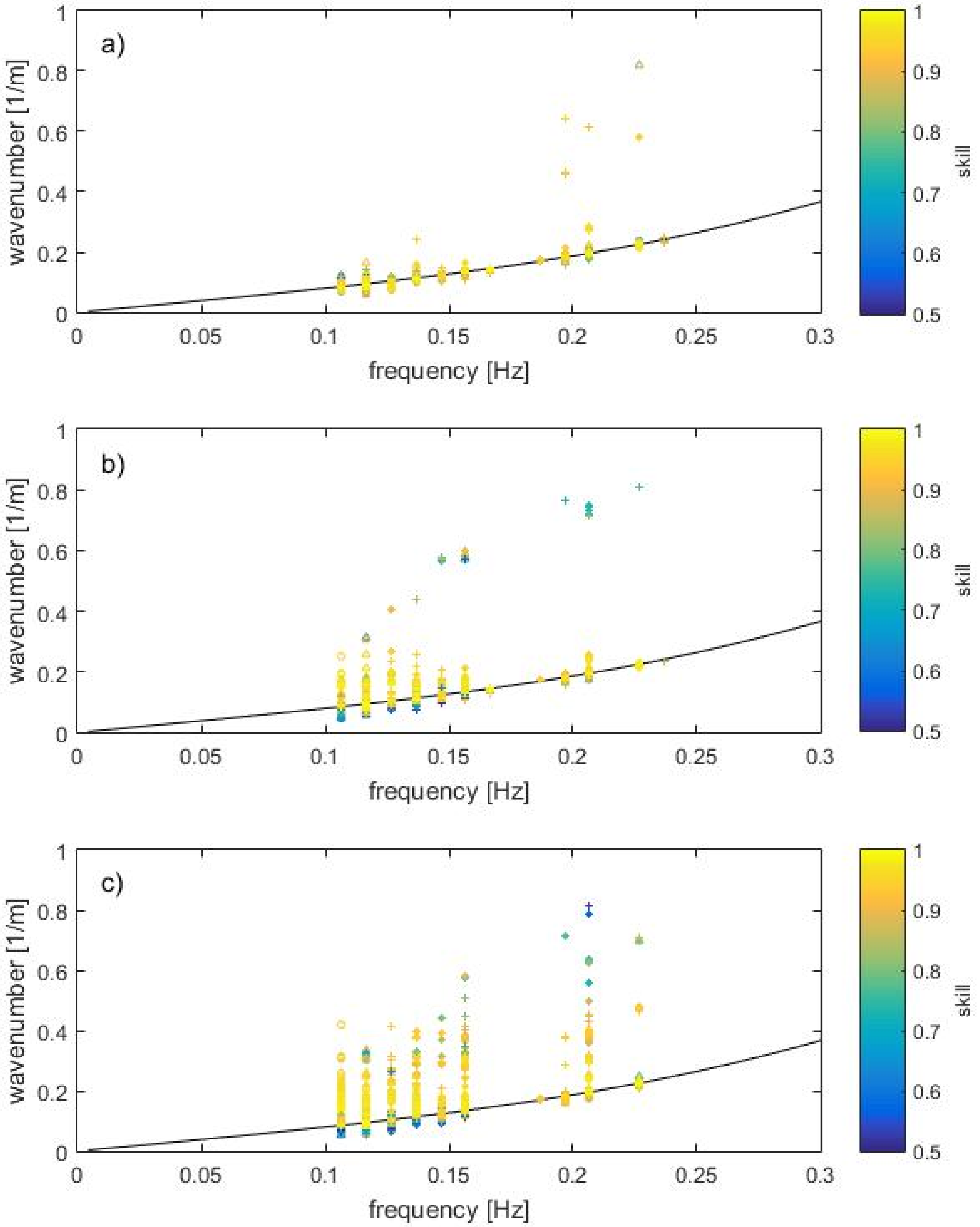

***Figure A.2** – Frequency and wavenumber pairs estimated from cBathy for case E01 and relative to waves coming from 0° and seed equal to 0° (a), 45° (b) and 90° (c). The curve shows the linear dispersion relationship for the specified water depth (7m). The markers indicate the f-k pairs estimated from cBathy in each point of the analysis grid and relative to the first (•), the second (△), the third (*) and the fourth (+) coherent frequency. The color gradient of the markers is proportional to the skill but only points that exceed the threshold are plotted. (For interpretation of the references to color in this figure legend, the reader is referred to the Web version of this article.)*